

# Higgs inflation puts lower and upper bounds on tensor-to-scalar ratio and on Higgs-portal-dark-matter mass

Yuta Hamada,<sup>\*1,2</sup> Hikaru Kawai,<sup>†3</sup> Yukari Nakanishi,<sup>‡4</sup> and Kin-ya Oda<sup>§4</sup>

<sup>1</sup>*Department of Physics, University of Wisconsin, Madison, WI 53706, USA*

<sup>2</sup>*KEK Theory Center, IPNS, KEK, Tsukuba, Ibaraki 305-0801, Japan*

<sup>3</sup>*Department of Physics, Kyoto University, Kyoto 606-8502, Japan*

<sup>4</sup>*Department of Physics, Osaka University, Osaka 560-0043, Japan*

July 2, 2022

## Abstract

We find a theoretical lower bound on the tensor-to-scalar ratio  $r$  from a premise that extrapolation of the Higgs-field direction plays the role of the inflaton at high scales. We assume that all the non-minimal couplings are not particularly large,  $\xi \lesssim 10^2$ , so that the renormalizable low-energy effective field theory is reliable up to  $10^{17}$  GeV ( $\lesssim M_{\text{P}}/\sqrt{\xi}$ ). This framework includes the so-called critical Higgs inflation. In our analysis, we take into account the Higgs-portal scalar dark matter and the heavy right-handed neutrinos. The resultant bounds are rather stringent. In particular in the absence of the right-handed neutrinos, namely, when the right-handed-neutrino masses are smaller than  $10^{13}$  GeV, the Planck bound  $r < 0.09$  implies that the dark-matter mass must be smaller than 1.2 TeV. On the other hand, the PandaX-II bound on the dark-matter mass  $m_{\text{DM}} \gtrsim 750$  GeV leads to  $r \gtrsim 4 \times 10^{-3}$ . Both are within the range of near-future detection. When we include the right-handed neutrinos of mass  $M_{\text{R}} \sim 10^{14}$  GeV, the allowed region becomes wider, but we still predict  $r \gtrsim 10^{-3}$  in the most of the parameter space. The most conservative bound becomes  $r > 10^{-5}$  if we allow three-parameter tuning of  $m_{\text{DM}}$ ,  $M_{\text{R}}$ , and the top-quark mass.

---

\*yhamada@wisc.edu

†hkawai@gauge.scphys.kyoto-u.ac.jp

‡nakanishi@het.phys.sci.osaka-u.ac.jp

§odakin@phys.sci.osaka-u.ac.jp

# Contents

<b>1</b>	<b>Introduction</b>	<b>3</b>
<b>2</b>	<b>Lower bound on tensor-to-scalar ratio</b>	<b>4</b>
<b>3</b>	<b><math>Z_2</math> Higgs-portal scalar model</b>	<b>5</b>
<b>4</b>	<b>Analysis without heavy right-handed neutrinos</b>	<b>6</b>
4.1	Method of analysis . . . . .	6
4.2	Results . . . . .	6
<b>5</b>	<b>Analysis with right-handed neutrinos</b>	<b>7</b>
5.1	Method of analysis . . . . .	7
5.2	Results for Normal Hierarchy . . . . .	8
5.3	Results for Inverted Hierarchy . . . . .	11
5.4	Results for Degenerate case . . . . .	13
<b>6</b>	<b>Allowed region for all parameter space</b>	<b>14</b>
6.1	Lower bound on $r$ for each $M_R$ . . . . .	14
6.2	Lower bound on $r$ for each $m_t$ . . . . .	15
<b>7</b>	<b>Summary and discussion</b>	<b>19</b>
<b>A</b>	<b>Renormalization group equations</b>	<b>20</b>
<b>B</b>	<b>Explaining the form of envelope by potential shape</b>	<b>22</b>

# 1 Introduction

We have seen remarkable development on the observation of the cosmic microwave background fluctuation. Currently the tensor-to-scalar ratio and the spectral index are fixed and bound as  $n_s = 0.968 \pm 0.006$  ( $1\sigma$ ) and  $r \leq 0.09$  ( $2\sigma$ ), respectively [1], and the single-field slow-roll inflation paradigm has been established, in which the Higgs inflation [2, 3] is one of the best-fit models. The Higgs field is the only elementary scalar whose existence is experimentally confirmed. Within the Standard Model (SM), the Higgs potential can be very small and flat around the Planck scale  $M_{\text{P}} = 1/\sqrt{8\pi G} \simeq 2.4 \times 10^{18}$  GeV, see e.g. Refs. [4, 5, 6, 7, 8, 9, 10, 11, 12, 13, 14, 15, 16, 17], and this fact suggests that the Higgs field plays the role of inflaton [18, 19].

In this paper, we assume that the Higgs field indeed serves as an inflaton above a scale  $\Lambda$  below which we may trust the renormalizable low-energy effective field theory; see Fig. 1. That is, above  $\Lambda$ , the potential of the Higgs field becomes flat and the slow-roll inflation is realized [18, 19]. The so-called critical Higgs inflation with non-minimal coupling  $\xi \lesssim 10^2$  [20, 21, 22, 23] is a concrete realization of this idea, which leads to  $\Lambda \sim M_{\text{P}}/\sqrt{\xi}$ .

When all the non-minimal couplings are not particularly large,  $\xi < 10^2$ , the renormalizable low-energy effective field theory is reliable up to  $10^{17}$  GeV. Hereafter, we take  $\Lambda = 10^{17}$  GeV, which is also the typical string scale. The dynamics above  $\Lambda$  can be anything as far as it realizes an inflation along a field direction that is extrapolated from the low-energy Higgs field [18, 19].

After the end of the inflation, the slow-roll condition on the Higgs field is violated and the field rolls on the potential hill down to the electroweak (EW) scale. In order not to prevent the rolling, the potential height must be smaller than the inflation energy  $V_{\text{inf}}$  in the whole region  $\varphi \leq \Lambda$ . Note that even if there exists a local maximum with its height smaller than  $V_{\text{inf}}$ , it should not prevent the rolling down to the EW scale because the slow-roll condition is already violated.

As we do not specify the inflaton potential above  $\Lambda$ , we cannot predict precisely the cosmological parameters such as the spectral index  $n_s$  and the tensor-to-scalar ratio  $r$ . However, we may still put a lower bound on  $V_{\text{inf}}$  from the highest value of the Higgs potential in the region  $\varphi < \Lambda$ , which can be converted into the lower bound on  $r$ .

It is certain that there exists a dark matter (DM). In this paper, we take a Higgs-portal  $Z_2$  scalar field as one of the simplest realizations. We consider the generic region of the DM mass  $m_{\text{DM}}$  being larger than the Higgs mass. Then its thermal abundance fixes the relation between the DM mass and the Higgs-DM coupling  $\kappa$  to be  $m_{\text{DM}} \simeq \kappa \times 3.2$  TeV, and the spin-independent DM-nucleon elastic cross section is fixed to be  $\sigma_{\text{SI}} = 8.4 \times 10^{-46}$  cm<sup>2</sup> [24, 25].

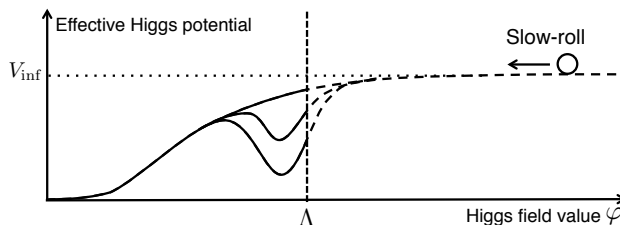


Figure 1: Schematic figure for the Higgs field as an inflaton

The latest  $1.6\sigma$  bound from the XENON1T experiment [26] reads  $m_{\text{DM}} \gtrsim 630 \text{ GeV}$ .<sup>1</sup> When we do not include the right-handed neutrinos, we find that the current observational bounds  $r < 0.09$  and  $m_{\text{DM}} \gtrsim 630 \text{ GeV}$  lead to the theoretical bounds  $m_{\text{DM}} \lesssim 1.2 \text{ TeV}$  and  $r \gtrsim 10^{-3}$ , respectively, which are well within the range of near future detection.

We have also studied the case with the right-handed neutrinos that account for the observed neutrino oscillations through the seesaw mechanism [29, 30]. We find that when their mass is in the range  $M_{\text{R}} \lesssim 10^{13} \text{ GeV}$ , the results are the same as in the case without them. As we increase  $M_{\text{R}}$ , the bound becomes milder up to the scale  $10^{14} \text{ GeV}$ , and then becomes tighter up to  $10^{15} \text{ GeV}$  at which the right-handed neutrino contribution makes the Higgs potential unstable. Combining these results, we find the absolute theoretical bound  $r > 10^{-5}$ . If we restrict  $m_{\text{DM}} \gtrsim 1.3 \text{ TeV}$ , we obtain a stronger bound  $r \gtrsim 10^{-3}$  for a reasonable top-quark mass range, as we will see in Fig. 6.

This paper is organized as follows. In Sec. 2, we show our basic strategy how to put a lower bound on  $r$  without the knowledge of higher scales. In Sec. 3, we review the Higgs-portal  $Z_2$  scalar dark matter. In Sec. 4, we show our results without the effects from the heavy right-handed neutrinos. In Sec. 5, we show the results with the right-handed neutrinos for several representative values of their mass  $M_{\text{R}}$ . In Sec. 6, we show the allowed region when we vary both  $M_{\text{R}}$  and the top-quark mass  $m_t$ . In Sec. 7, we summarize and discuss our results. In Appendix A, we show the renormalization group equations (RGEs) that we employ in the computation of the effective potential. In Appendix B, we discuss that the shape of allowed region, shown in Secs. 4–6, can be understood in terms of the difference of potential shape.

## 2 Lower bound on tensor-to-scalar ratio

We present our basic strategy how to put a lower bound on  $r$  without the knowledge of the physics at the higher Higgs-field value  $\varphi > \Lambda$ , extending the analysis in Ref. [18]. In the slow-roll inflation, the observable  $A_s$  and  $r$  are written in terms of  $\epsilon_V$  and  $V_{\text{inf}}$ :

$$A_s = \frac{1}{24\pi^2} \frac{1}{\epsilon_V} \frac{V_{\text{inf}}}{M_{\text{P}}^4}, \quad r = 16\epsilon_V, \quad (1)$$

where

$$\epsilon_V := \frac{M_{\text{P}}^2}{2} \left( \frac{V_{,\varphi}}{V} \right)^2, \quad (2)$$

is the slow-roll parameter. Eliminating  $\epsilon_V$ , we obtain

$$r = \frac{2}{3\pi^2} \frac{1}{A_s} \frac{V_{\text{inf}}}{M_{\text{P}}^4}. \quad (3)$$

This gives a linear relation between  $r$  and  $V_{\text{inf}}$  since  $A_s$  is fixed by the CMB observation to be  $A_s \simeq 2.2 \times 10^{-9}$  [31].

During the inflation, the inflaton field value is larger than  $\Lambda$ ; see Fig. 1. After the end of inflation, the field continues to roll down the potential hill and becomes the low-energy Higgs field that we know in the SM. In order not to prevent the rolling down to the EW scale, the

---

<sup>1</sup> The  $1.6\sigma$  results from the LUX [27] and PandaX-II [28] experiments imply  $m_{\text{DM}} \gtrsim 400 \text{ GeV}$  and  $m_{\text{DM}} \gtrsim 750 \text{ GeV}$  (preliminary), respectively.

maximum value of the effective potential in the region  $\varphi \leq \Lambda$ , which we call  $V_{\varphi \leq \Lambda}^{\max}$ , must be smaller than the energy density during the inflation  $V_{\text{inf}}$ :

$$V_{\varphi \leq \Lambda}^{\max} < V_{\text{inf}}. \quad (4)$$

From Eqs. (3) and (4),

$$r > r_{\text{bound}} := \frac{2}{3\pi^2} \frac{1}{A_s} \frac{V_{\varphi \leq \Lambda}^{\max}}{M_{\text{P}}^4}. \quad (5)$$

Thus, we obtain the lower bound on  $r$  from  $V_{\varphi \leq \Lambda}^{\max}$  only.

### 3 $Z_2$ Higgs-portal scalar model

In this paper, we employ the Higgs-portal  $Z_2$  scalar dark matter. Below the scale  $\Lambda$  our Lagrangian is

$$\mathcal{L} = \mathcal{L}_{\text{SM}} + \frac{1}{2}(\partial_\mu S)^2 - \frac{1}{2}m_S^2 S^2 - \frac{\lambda_S}{4!} S^4 - \frac{\kappa}{2} S^2 \Phi^\dagger \Phi, \quad (6)$$

where  $\Phi$  is the SM Higgs doublet and  $S$  is the Higgs portal scalar field which has  $Z_2$  symmetry. Hereafter we use  $\varphi := \sqrt{2\Phi^\dagger \Phi}$ . The singlet  $S$  is identified as the DM, whose mass is

$$m_{\text{DM}}^2 = m_S^2 + \frac{\kappa v^2}{2}, \quad (7)$$

where  $v \simeq 246$  GeV is the Higgs vacuum expectation value (VEV). The parameters  $\lambda_S$  and  $\kappa$  affects  $V_{\varphi \leq \Lambda}$  through the renormalization group (RG) running of the Higgs quartic coupling, while  $m_S$  does not. We assume that  $S$  does not acquire a Planck scale VEV and thus does not affect the inflation.

In this model, the thermal abundance of the DM fixes the relation between  $\kappa$  and  $m_{\text{DM}}$  in the non-resonant region [24]

$$\log_{10} \kappa \simeq -3.63 + 1.04 \log_{10} \frac{m_{\text{DM}}}{\text{GeV}}. \quad (8)$$

This relation allows us to convert  $m_{\text{DM}}$  into  $\kappa$  and vice versa. In the region of our interest,  $0.1 \lesssim \kappa \lesssim 0.5$ , this roughly translates

$$m_{\text{DM}} \simeq \kappa \times 3.2 \text{ TeV}. \quad (9)$$

We will employ the pole mass of the top quark  $m_t$  as an input parameter for the RG analysis below. The Monte-Carlo mass of the top quark has been precisely measured to be  $m_t^{\text{MC}} = 173.1 \pm 0.6$  GeV [32]. However, the relation between  $m_t^{\text{MC}}$  and the pole mass  $m_t$  is still unclear, and there remains uncertainty at least of 1 GeV; see e.g. Ref. [33] for a recent review. A theorist's combination of the pole mass, derived from the cross-section measurements, reads  $m_t = 173.5 \pm 1.1$  GeV [32]. Hereafter we take conservatively two ranges:

$$171 \text{ GeV} < m_t < 176 \text{ GeV}, \quad (10)$$

$$169 \text{ GeV} < m_t < 178 \text{ GeV}, \quad (11)$$

which roughly corresponds to  $2\sigma$  and  $4\sigma$  ranges of the above combination, respectively.

## 4 Analysis without heavy right-handed neutrinos

As shown in the previous section, we need to compute  $V_{\varphi \leq \Lambda}$  in order to put the lower bound on  $r$ . We may find the excluded region in the  $r$ - $m_{\text{DM}}$  plane by obtaining  $V_{\varphi \leq \Lambda}^{\text{max}}$  as a function of  $\kappa$  for each fixed set of  $(\lambda_S, m_t)$  and converting  $\kappa$  to  $m_{\text{DM}}$  via Eq. (8). We first present our method of analysis in Sec. 4.1. Then we show our results in Sec. 4.2.

### 4.1 Method of analysis

We employ the two-loop RGEs, which are summarized in Appendix A. The input parameters for them are  $\lambda_S$ ,  $\kappa$ , and the pole mass of top quark  $m_t$ .<sup>2</sup> From the obtained running couplings, we determine  $V_{\varphi \leq \Lambda}$ . Then we exclude the parameter region in which  $V$  becomes negative in  $\varphi \leq \Lambda$  or the perturbativity of couplings is violated. For the perturbativity, we demand that all the couplings are smaller than  $\sqrt{4\pi} \simeq 3.5$  in all the region  $\varphi \leq \Lambda$ . This condition chooses the region  $\kappa \leq 0.5$  ( $m_{\text{DM}} \lesssim 1.6$  TeV) for  $\lambda_S = 0$ .<sup>3</sup> In this paper, we restrict to the case  $\lambda_S = 0$  except for the right of Fig. 2 in which we instead take  $\lambda_S = 0.6$  for comparison.<sup>4</sup>

For numerical computation, we first neglected the wave-function renormalization  $\Gamma(\varphi)$  given in Eq. (19). We have also estimated the largest possible deviation due to  $\Gamma(\varphi)$  by setting  $\varphi = \Lambda$ ; see Appendix A for details.

### 4.2 Results

We plot the allowed region in  $r$ - $m_{\text{DM}}$  plane for  $\lambda_S = 0$  in the left of Fig. 2. A solid and dashed lines denote the results without and with the effects of  $\Gamma$ , respectively, mentioned above. The region below each line is excluded, with its rainbow-color corresponding to each  $m_t$  value. In the right, we superimpose the excluded region for  $\lambda_S = 0.6$  on the envelope of the left for a comparison with larger value of  $\lambda_S$ . To understand the form of envelope, we need to know how the Higgs potential changes its shape with parameters, see Appendix B.<sup>5</sup>

Fig. 2 shows that the Planck constraint  $r < 0.09$  [1] leads to bounds on  $m_t$  and  $m_{\text{DM}}$ :

$$171 \text{ GeV} < m_t < 175 \text{ GeV}, \quad (12)$$

$$m_{\text{DM}} \lesssim 1.1 \text{ TeV}. \quad (13)$$

This bound on  $m_{\text{DM}}$  is stricter than the above-mentioned perturbativity bound  $m_{\text{DM}} \lesssim 1.6$  TeV.

If we take the lower bound from the XENON1T experiment [26],  $m_{\text{DM}} \gtrsim 630$  GeV ( $\kappa \gtrsim 0.19$ ), we obtain a lower bound:  $r \gtrsim 2 \times 10^{-4}$ . If we take the lower bound by the PandaX-II experiment [28],  $m_{\text{DM}} \gtrsim 750$  GeV ( $\kappa \gtrsim 0.23$ ), we obtain the lower bound on tensor-to-scalar ratio

$$r \gtrsim 4 \times 10^{-3}. \quad (14)$$

We can explore this possibility in near-future experiments such as the POLARBEAR-2 [34], LiteBIRD [35] and CORE [36].

<sup>2</sup> The couplings are given at the scale  $\mu = m_t$  unless otherwise stated.

<sup>3</sup> See Fig. 1 in Ref. [25] for the allowed region in the  $\lambda_S$ - $\kappa$  plane.

<sup>4</sup> We will see in the right of Fig. 2 that the large  $\lambda_S$  tends to narrower the allowed region. Therefore, it is more conservative to set  $\lambda_S = 0$ .

<sup>5</sup> The same explanation can be adapted for the other envelopes appearing hereafter.

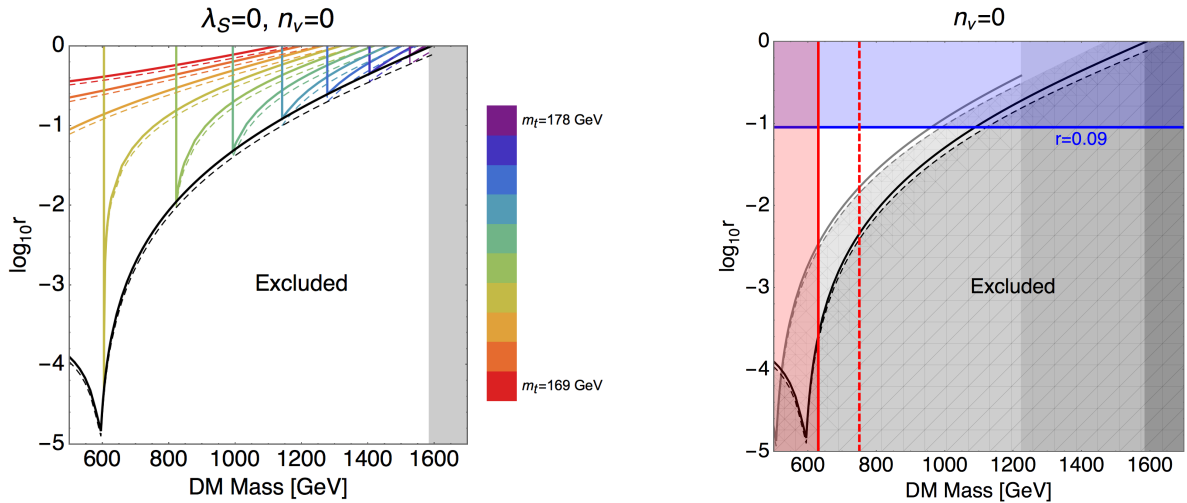


Figure 2: Left: Allowed regions for  $\lambda_S = 0$ . The region above each rainbow-colored line is allowed for a given  $m_t$ . Each vertical line denotes the lower bound on  $m_{\text{DM}}$  from the positivity of potential:  $V_{\varphi \leq \Lambda} > 0$ . The envelope of the rainbow-colored lines, indicated by the black line, gives the lower bound on  $r$  for each  $m_{\text{DM}}$  when one varies  $m_t$ . We have shaded the region  $m_{\text{DM}} \geq 1585$  GeV where perturbativity is violated. (See Fig. 8 for the corresponding plot with right-handed neutrinos.) Right: Excluded regions for  $\lambda_S = 0$  (below black line) and  $\lambda_S = 0.6$  (below gray line). The vertical black (gray) shade in  $m_{\text{DM}} \geq 1585$  GeV ( $m_{\text{DM}} \geq 1223$  GeV) is excluded by the perturbativity for  $\lambda_S = 0$  (0.6). The blue line denotes  $r = 0.09$  its the upper side is excluded [1]. The red lines denote the lower bounds on DM mass,  $m_{\text{DM}} = 630$  GeV from XENON1T [26] (solid) and  $m_{\text{DM}} = 750$  GeV from PandaX-II [28] (dashed).

## 5 Analysis with right-handed neutrinos

We introduce the heavy right-handed neutrinos that account for the observed neutrino masses through the seesaw mechanism, and obtain the lower bound on  $r$  for each DM mass.

### 5.1 Method of analysis

The observational constraints on mass of left-handed neutrinos are the upper bound on the sum of masses and their squared differences; see e.g. Ref. [37]. Under this condition, we consider the following three typical patterns of mass relations:

1. Normal Hierarchy (NH,  $m_1$  the lightest),
2. Inverted Hierarchy (IH,  $m_3$  the lightest),
3. Degenerate (all masses comparable).

The mass pattern is most hierarchical when the lightest one is 0. In Degenerate case, the upper bound on the sum of neutrino masses reads  $m_i \lesssim 0.1$  eV.<sup>6</sup> In Table 1, we show the

<sup>6</sup> The left-handed neutrino mass 0.1 eV for the three degenerate neutrinos corresponds to  $\sum_i m_i = 0.3$  eV. The  $2\sigma$  upper bound from the TT-only analysis is  $\sum_i m_i < 0.715$  eV, while that from the TT+lensing+ext gives  $\sum_i m_i < 0.234$  eV [1].

	$m_1$ [eV]	$m_2$ [eV]	$m_3$ [eV]	Pattern
1. Normal Hierarchy	0 (set)	$8.6 \times 10^{-3}$	$5.1 \times 10^{-2}$	$m_1 \ll m_2 < m_3$
2. Inverted Hierarchy	$5.0 \times 10^{-2}$	$5.0 \times 10^{-2}$	0 (set)	$m_1 \simeq m_2 \gg m_3$
3. Degenerate (NO)	0.1 (set)	$1.0 \times 10^{-1}$	$1.1 \times 10^{-1}$	$m_1 \simeq m_2 \simeq m_3$
3. Degenerate (IO)	$1.1 \times 10^{-1}$	$1.1 \times 10^{-1}$	0.1 (set)	$m_1 \simeq m_2 \simeq m_3$

Table 1: Neutrino masses obtained from the absolute values of mass-squared differences in the notation of Ref. [37].

	Number of effective $\nu$	Common mass $m_\nu$ [eV]
1. Normal Hierarchy	$n_\nu = 1$	$5.1 \times 10^{-2}$
2. Inverted Hierarchy	$n_\nu = 2$	$5.0 \times 10^{-2}$
3. Degenerate	$n_\nu = 3$	$1.1 \times 10^{-1}$

Table 2: Common neutrino mass that we use as an input.

mass pattern by setting the lightest one to be zero (0.1 eV) for the cases of normal/Inverted Hierarchy (Degenerate), using the mass-squared differences in Ref. [37]. For the three cases, we approximate the heaviest  $n_\nu$  neutrinos as having a common mass  $m_\nu$  and the remaining  $3 - n_\nu$  ones as being massless as shown in Table 2.<sup>7</sup>

Under the existence of heavy right-handed neutrino, the remaining input parameters to determine  $V_{\varphi \leq \Lambda}$  are  $\lambda_S$ ,  $\kappa$ ,  $m_t$ , and the right-handed neutrino mass  $M_{R,i}$ . For simplicity, we assume that  $M_{R,i}$  ( $i = 1, 2, 3$ ) are identical:  $M_{R,i} = M_R$ . The Yukawa coupling of neutrino is given by the seesaw mechanism:  $y_\nu = \sqrt{2m_\nu M_R}/v$ , with  $v \simeq 246$  GeV. We show the  $\beta$ -functions in this case in Appendix A.

## 5.2 Results for Normal Hierarchy

We show the results for Normal Hierarchy,  $n_\nu = 1$ , in Fig. 3. The right-handed neutrino mass  $M_R$  is fixed in each panel:  $10^{13}$ ,  $10^{14}$ ,  $10^{14.4}$  ( $\simeq 2.5 \times 10^{14}$ ),  $10^{14.5}$  ( $\simeq 3.2 \times 10^{14}$ ),  $10^{14.6}$  ( $\simeq 4.0 \times 10^{14}$ ), and  $10^{14.7}$  ( $\simeq 5.0 \times 10^{14}$ ) in units of GeV. The color of envelope in each panel, denoted by the thick line, corresponds to the color in the plots in Sec. 6, in which the discussion for more general values of  $M_R$  will be given. Note that the thick line is obtained by tuning one parameter  $m_t$  for fixed  $M_R$ , and its minimum corresponds to the two parameter

<sup>7</sup> If we want to consider a different  $m_\nu$ , we may simply rescale the right-handed neutrino mass  $M_R$  in our results, since  $m_\nu \propto M_R^{-1}$  by the seesaw mechanism.

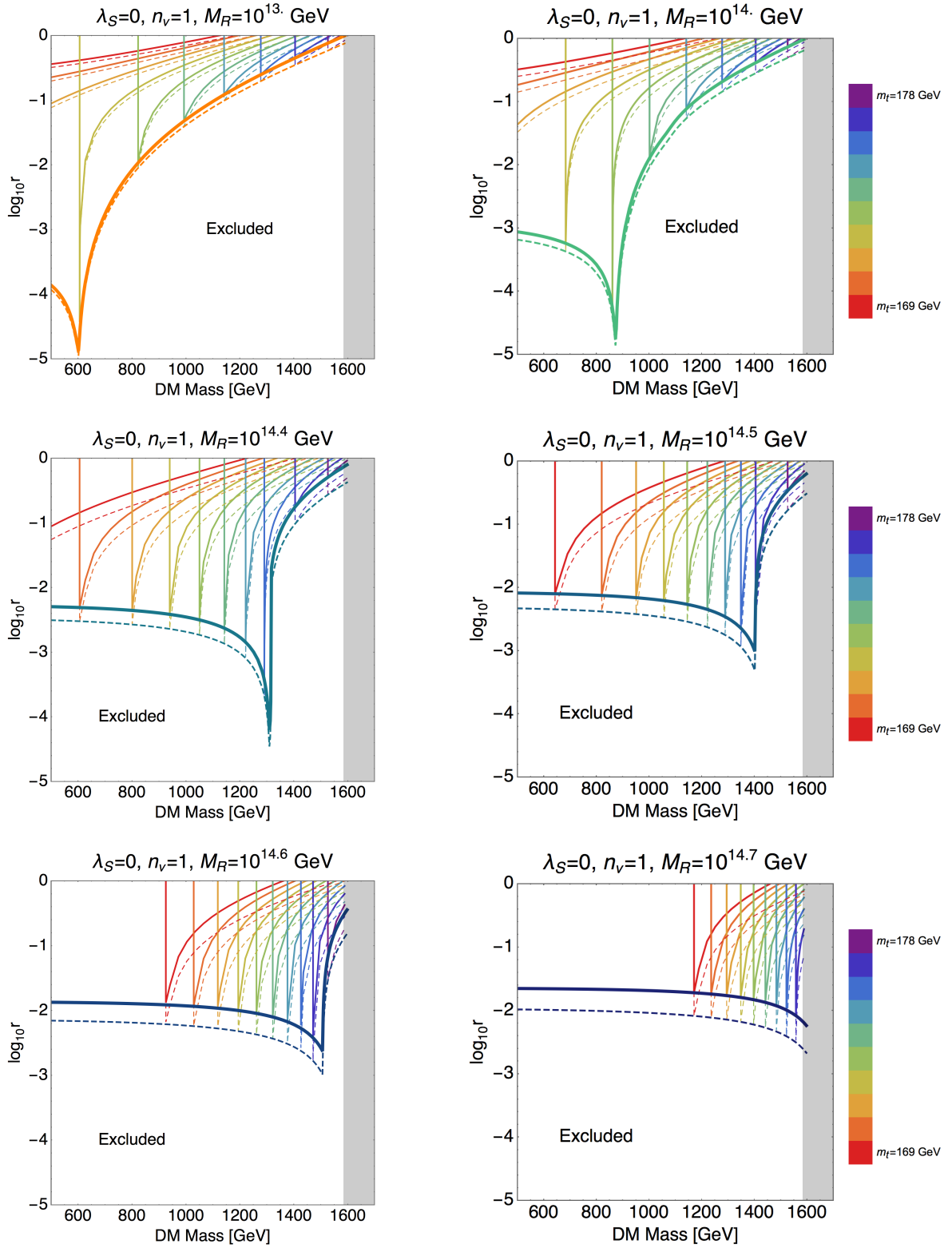


Figure 3: Allowed region for Normal Hierarchy with  $\lambda_S = 0$ . The right-handed neutrino mass  $M_R$  is increased in the order of the upper-left, upper-right, middle-left, . . . , lower-right panels. The bold line in each panel is the envelope of the  $m_t$ -fixed rainbow-colored lines, and gives the lower bound on  $r$  for the fixed  $M_R$ . See the caption of Fig. 2 for the shaded region.

	$m_t$	$M_R$
$m_{\text{DM}} = 1 \text{ TeV}, r = 0.01$	$m_t < 174 \text{ GeV}$	$10^{14} \text{ GeV} \lesssim M_R \lesssim 10^{14.6} \text{ GeV}$
$m_{\text{DM}} = 1 \text{ TeV}, r = 0.001$	$173 \text{ GeV} < m_t < 174 \text{ GeV}$	$10^{14.1} \text{ GeV} \lesssim M_R \lesssim 10^{14.3} \text{ GeV}$
$m_{\text{DM}} = 1.5 \text{ TeV}, r = 0.01$	$170 \text{ GeV} < m_t < 178 \text{ GeV}$	$10^{14.6} \text{ GeV} \lesssim M_R \lesssim 10^{14.8} \text{ GeV}$
$m_{\text{DM}} = 1.5 \text{ TeV}, r = 0.001$	$m_t \simeq 177.8 \text{ GeV}$	$M_R \simeq 10^{14.6} \text{ GeV}$

Table 3: Constraints that will be obtained from future observations of  $m_{\text{DM}}$  and  $r$  for Normal Hierarchy.

tuning of  $m_t$  and  $m_{\text{DM}}$ .

With the right-handed neutrino, we have one more theoretical parameter  $M_R$  in addition to  $m_t$  to determine from the observational constraints of  $r$  and  $m_{\text{DM}}$ . From Fig. 3, we see that the larger the  $M_R$  is, the smaller the allowed region becomes, for a given lower bound on  $m_t$ . This is because the right-handed neutrinos and the top quark have a similar effect on the Higgs potential, namely, they drives the Higgs quartic coupling smaller through the RG running towards high scales, and therefore they tend to make the Higgs potential negative if they both are heavy.<sup>8</sup> If we e.g. set  $m_t > 169 \text{ GeV}$ , we have the constraint  $M_R \lesssim 10^{14.8} \text{ GeV}$  ( $\simeq 6.3 \times 10^{14} \text{ GeV}$ ); see also Fig. 7 in Sec. 6.

As we increase  $M_R$  and switch panels in Fig. 3, we see that the value of  $m_{\text{DM}}$  at the minimum point of the envelope becomes larger: 600 GeV, 870 GeV, etc. In particular, it goes beyond the perturbativity bound, indicated by the gray band, when  $M_R = 10^{14.7} \text{ GeV}$ . Therefore, if the right-handed neutrino mass is larger than that, we have a stringent lower bound:  $r \gtrsim 10^{-2}$ . On the other hand, the plot with  $M_R \lesssim 10^{13} \text{ GeV}$  is almost the same as the case without right-handed neutrinos shown in the left of Fig. 2.

Let us see implications of future discoveries of the DM and  $r$ :<sup>9</sup>

- Suppose that  $m_{\text{DM}} = 1 \text{ TeV}$  ( $\kappa \simeq 0.31$ ) and  $r = 0.01$  are found. Then the right-handed neutrino mass is predicted to be in the narrow range  $10^{14} \text{ GeV} \lesssim M_R \lesssim 10^{14.6} \text{ GeV}$  and the top-quark mass is constrained from above:  $m_t < 174 \text{ GeV}$ .
- If we discover  $m_{\text{DM}} = 1.5 \text{ TeV}$  ( $\kappa \simeq 0.47$ ) and  $r = 0.01$ , we obtain the theoretical lower bound  $M_R \gtrsim 10^{14.6} \text{ GeV}$ , while the top quark mass is less constrained:  $171 \text{ GeV} < m_t < 178 \text{ GeV}$ . However,  $M_R$  and  $m_t$  are highly correlated in this case. Therefore if one of them is fixed, the other is precisely predicted.
- See Table 3 for other pairs of  $m_{\text{DM}}$  and  $r$ . Generically the heavy DM mass tends to predict the heavy top-quark mass and  $M_R$ . The smaller the  $r$  is, the tighter the range of

<sup>8</sup> In this case, the vacuum stability is violated before the perturbativity.

<sup>9</sup> Here, we fit  $M_R$  and  $m_t$  from the future observation of  $m_{\text{DM}}$  and  $r$ . Instead, one might narrow down the error on the pole mass  $m_t$  e.g. at the High Luminosity LHC (HL-LHC) [38]. Then one may use  $m_t$  and  $m_{\text{DM}}$  as input parameters to predict  $M_R$  and  $r$ .

$m_t$ . Especially, if we discover  $m_{\text{DM}} = 1.5 \text{ TeV}$  and  $r = 0.001$ ,  $m_t$  and  $M_{\text{R}}$  are accurately predicted.

We can predict  $r_{\text{bound}}$  or  $m_{\text{DM}}$  to some extent by considering typical input parameters. When we choose  $m_t = 173 \text{ GeV}$  and  $M_{\text{R}} = 10^{14} \text{ GeV}$ , we obtain the bound  $m_{\text{DM}} \sim 860 \text{ GeV} - 970 \text{ GeV}$  for  $r < 0.09$ .

### 5.3 Results for Inverted Hierarchy

We show the results for the case of Inverted Hierarchy ( $n_\nu = 2$ ) in Fig. 4. In this case, the right-handed neutrinos lighter than  $\sim 10^{13} \text{ GeV}$  do not affect the analysis, similarly as in the case of Normal Hierarchy. However, the upper bound on  $M_{\text{R}}$  is slightly different:  $M_{\text{R}} \lesssim 10^{14.7} \text{ GeV}$ , see also Fig. 6. Let us summarize implications of future discoveries of the DM and  $r$  again:

- If we discover  $m_{\text{DM}} = 1 \text{ TeV}$  and  $r = 0.01$ , we obtain  $10^{13.9} \text{ GeV} \lesssim M_{\text{R}} \lesssim 10^{14.4} \text{ GeV}$  and  $m_t < 174 \text{ GeV}$ .
- If we discover  $m_{\text{DM}} = 1.5 \text{ TeV}$  and  $r = 0.01$ ,  $M_{\text{R}}$  must be larger than  $\sim 10^{14.6} \text{ GeV}$  and  $170 \text{ GeV} < m_t < 178 \text{ GeV}$ . Although we cannot obtain the global narrow bounds on  $M_{\text{R}}$  and  $m_t$ , they are highly correlated as in the case of Normal Hierarchy.

See Table 4 for other pairs of  $m_{\text{DM}}$  and  $r$ .

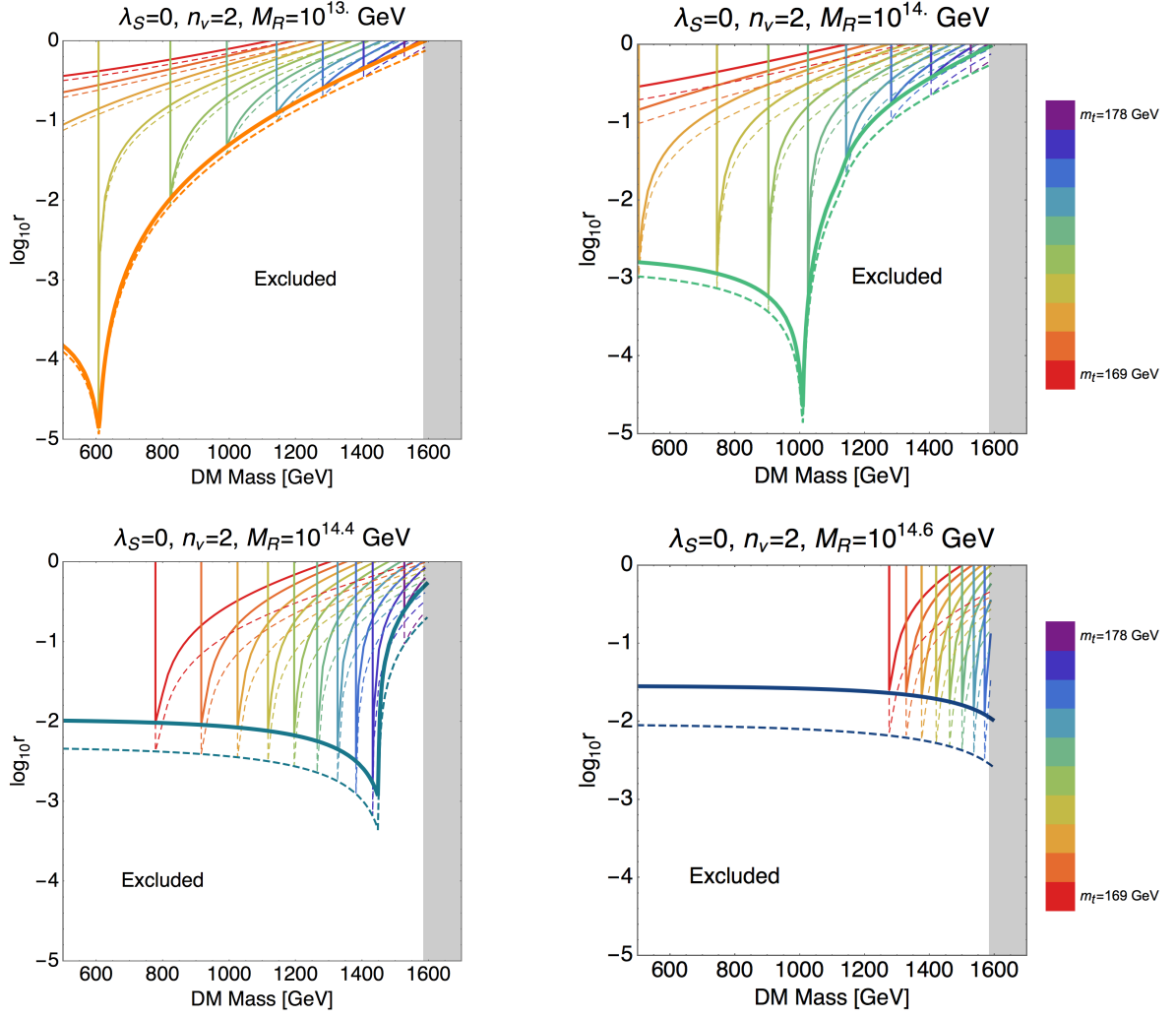


Figure 4: Allowed region for Inverted Hierarchy with  $\lambda_S = 0$ . See caption of Fig. 3 for the explanation.

	$m_t$	$M_R$
$m_{\text{DM}} = 1 \text{ TeV}, r = 0.01$	$m_t < 174 \text{ GeV}$	$10^{13.9} \text{ GeV} \lesssim M_R < 10^{14.5} \text{ GeV}$
$m_{\text{DM}} = 1 \text{ TeV}, r = 0.001$	$173 \text{ GeV} < m_t < 174 \text{ GeV}$	$10^{13.9} \text{ GeV} < M_R < 10^{14.2} \text{ GeV}$
$m_{\text{DM}} = 1.5 \text{ TeV}, r = 0.01$	$m_t < 178 \text{ GeV}$	$10^{14.4} \text{ GeV} < M_R \lesssim 10^{14.7} \text{ GeV}$
$m_{\text{DM}} = 1.5 \text{ TeV}, r = 0.001$	$177 \text{ GeV} < m_t < 178 \text{ GeV}$	$10^{14.4} \text{ GeV} < M_R < 10^{14.5} \text{ GeV}$

Table 4: Constraints obtained for Inverted Hierarchy.

## 5.4 Results for Degenerate case

We show the results for Degenerated case ( $n_\nu = 3$ ) in Fig. 5. The right-handed neutrinos lighter than  $\sim 10^{13}$  GeV do not affect the analysis, similarly as other cases. The upper bound on  $M_R$  is smaller than in other cases:  $M_R \lesssim 10^{14.2}$  GeV  $\simeq 1.6 \times 10^{14}$  GeV.

We summarize implications of future discoveries  $m_{\text{DM}}$  and  $r$  in Table 5. The right-handed neutrino mass tend to be lighter than hierarchical cases due to the heavy  $m_\nu$ . However, the prediction of  $m_t$  is similar to the other cases.

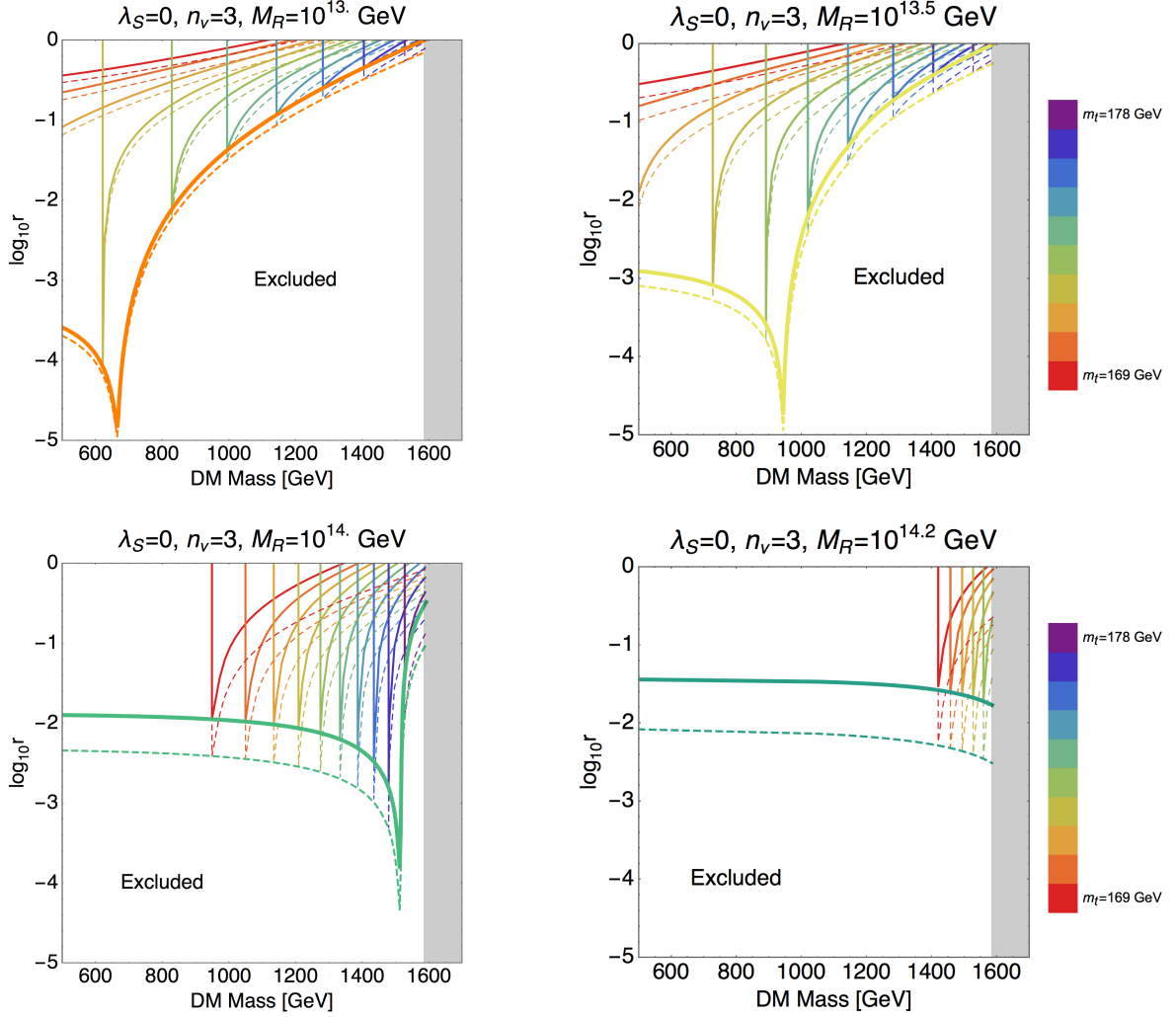


Figure 5: Allowed region for Degenerate case with  $\lambda_S = 0$ . See caption of Fig. 3 for the explanation.

	$m_t$	$M_R$
$m_{\text{DM}} = 1 \text{ TeV}, r = 0.01$	$m_t < 174 \text{ GeV}$	$10^{13.5} \text{ GeV} \lesssim M_R \lesssim 10^{14} \text{ GeV}$
$m_{\text{DM}} = 1 \text{ TeV}, r = 0.001$	$173 \text{ GeV} \lesssim m_t < 174 \text{ GeV}$	$10^{13.5} \text{ GeV} < M_R < 10^{13.8} \text{ GeV}$
$m_{\text{DM}} = 1.5 \text{ TeV}, r = 0.01$	$m_t < 178 \text{ GeV}$	$10^{14} \text{ GeV} \lesssim M_R \lesssim 10^{14.2} \text{ GeV}$
$m_{\text{DM}} = 1.5 \text{ TeV}, r = 0.001$	$176 \text{ GeV} < m_t < 178 \text{ GeV}$	$M_R \simeq 10^{14} \text{ GeV}$

Table 5: Constraints obtained for degenerate case.

## 6 Allowed region for all parameter space

In the previous section, we have plotted the bounds for various  $m_t$  in each panel of fixed  $M_R$ . In each panel, we have also shown the envelope of different  $m_t$  lines. This envelope is our theoretical lower bound on  $r$  for a given  $M_R$ .

In Sec. 6.1, we show these envelopes altogether in the same plot, and give the absolute lower bound on  $r$  for varying  $m_t$  and  $M_R$ . In Sec. 6.2, we see the same absolute lower bound in a different way, by changing the order of fixing  $m_t$  and  $M_R$ .

### 6.1 Lower bound on $r$ for each $M_R$

In Figs. 6 and 7, we plot our theoretical lower bounds on  $r$  for various  $M_R$  when we allow the top-quark pole mass within roughly  $2\sigma$  and  $4\sigma$  ranges shown in Eqs. (10) and (11), respectively. We also give the envelope of these lines, which gives the allowed region for varying  $m_t$  and  $M_R$ . In the plot, each colored line represents the lower bound on  $r$ , and corresponds to the envelope denoted by the thick colored line in Secs. 5.2–5.4. We also show the absolute lower bound by the black line.<sup>10</sup>

We explain the envelope denoted by the black line in Fig. 6:

- We see that the allowed region is enlarged to

$$r \gtrsim 10^{-5} \quad (15)$$

from the  $n_\nu = 0$  case in Eq. (14), which is read from the black line in Fig. 2 (being close the orange  $M_R = 10^{13} \text{ GeV}$  line in Fig. 6). This is because the loop corrections of heavy right-handed neutrinos reduce  $V_{\varphi \leq \Lambda}^{\text{max}}$ .

<sup>10</sup> We have plotted the envelope, denoted by the black line, as follows: 1) Each  $M_R$ -fixed line has a minimum. Make an interpolating function which linearly join all these minimum points. 2) Each  $m_t$ -fixed line has a minimum. Make another interpolating function which linearly join all these minimum points. 3) Make a function that chooses the smaller value of these two for each  $m_{\text{DM}}$ . 4) In large  $m_{\text{DM}}$  region, we replace the interpolated bound with the lower bound determined by the maximal  $m_t$ ; see the caption of Fig. 8 to see how  $m_t$  gives the bound. Note that these interpolating functions are evaluated only for  $600 \text{ GeV} < m_{\text{DM}} < 1600 \text{ GeV}$ , and hence they are untrustworthy in the extrapolated regions  $m_{\text{DM}} < 600 \text{ GeV}$  and  $m_{\text{DM}} > 1600 \text{ GeV}$ . This does not do any harm because these regions are already excluded by the direct DM search and by the perturbativity, respectively.

- The lower bound on  $r$  increases rapidly in the region  $m_{\text{DM}} \gtrsim 1.3 \text{ TeV}$  due to the upper end of the parameter  $m_t < 176 \text{ GeV}$ .
- In the region near the envelope denoted by the black line, the two input parameters  $m_t$  and  $M_{\text{R}}$  are simultaneously tuned to minimize the potential height  $V_{\varphi \leq \Lambda}^{\text{max}}$ .
- If one allows to adjust the three parameters,  $m_t$ ,  $M_{\text{R}}$ , and  $m_{\text{DM}}$  simultaneously, then the lowest point of the black line,  $r \sim 10^{-5}$ , is realized. This might be the case if some logic that demands the fine tuning, such as the multiple-point principle [39, 40, 41], is indeed applicable.

In Fig. 7, we plot for a wider range of the top-quark mass (11). The lower bound on  $r$ , denoted by the black line, increases in the region  $m_{\text{DM}} \gtrsim 1.3 \text{ TeV}$  in the cases of  $n_\nu = 1$  and 2 because of the difference of potential shapes explained in Appendix B, while its rise in the region  $m_{\text{DM}} \gtrsim 1.5 \text{ TeV}$  is due to the upper end of the parameter  $m_t < 178 \text{ GeV}$ .

## 6.2 Lower bound on $r$ for each $m_t$

In Fig. 8, we show the lower bound on  $r$  for each fixed  $m_t$  with  $M_{\text{R}}$  being varied. The envelope, denoted by the black line, is the same as the global lower bound on  $r$  in Sec. 6.1 except for the range explained in the caption.

The lowest possible value of  $m_{\text{DM}}$  for each  $m_t$  does not depend on the number of neutrinos  $n_\nu$ . Therefore, for any given lower bound on  $m_t$ , we obtain the corresponding lower bound of  $m_{\text{DM}}$  without any assumptions on the other parameters in the neutrino sector. We see that the lowest point for a given  $m_t$  moves right as we increase  $m_t$ . This leads to a strong correlation between  $m_t$  and  $m_{\text{DM}}$  regardless of  $n_\nu$  if  $r < 10^{-3}$ .

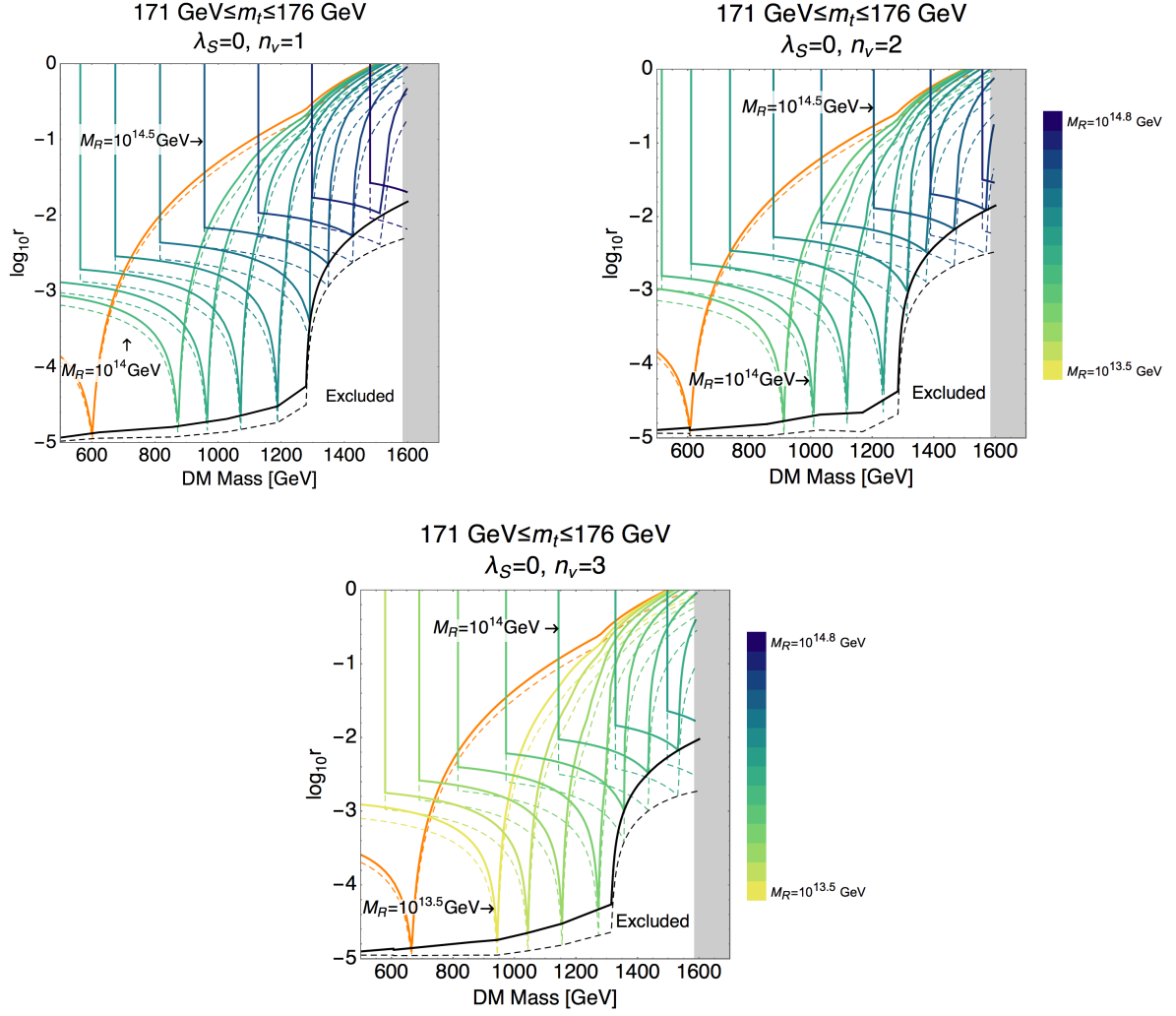


Figure 6: The lower bound on  $r$  for each fixed  $M_R$  (colored) and the envelope (black) with  $\lambda_S = 0$  and  $171 \text{ GeV} < m_t < 176 \text{ GeV}$ . The orange line is for  $M_R = 10^{13} \text{ GeV}$ . The vertical colored line comes from the lower end,  $m_t > 171 \text{ GeV}$ . See the caption of Fig. 2 for the shaded region.

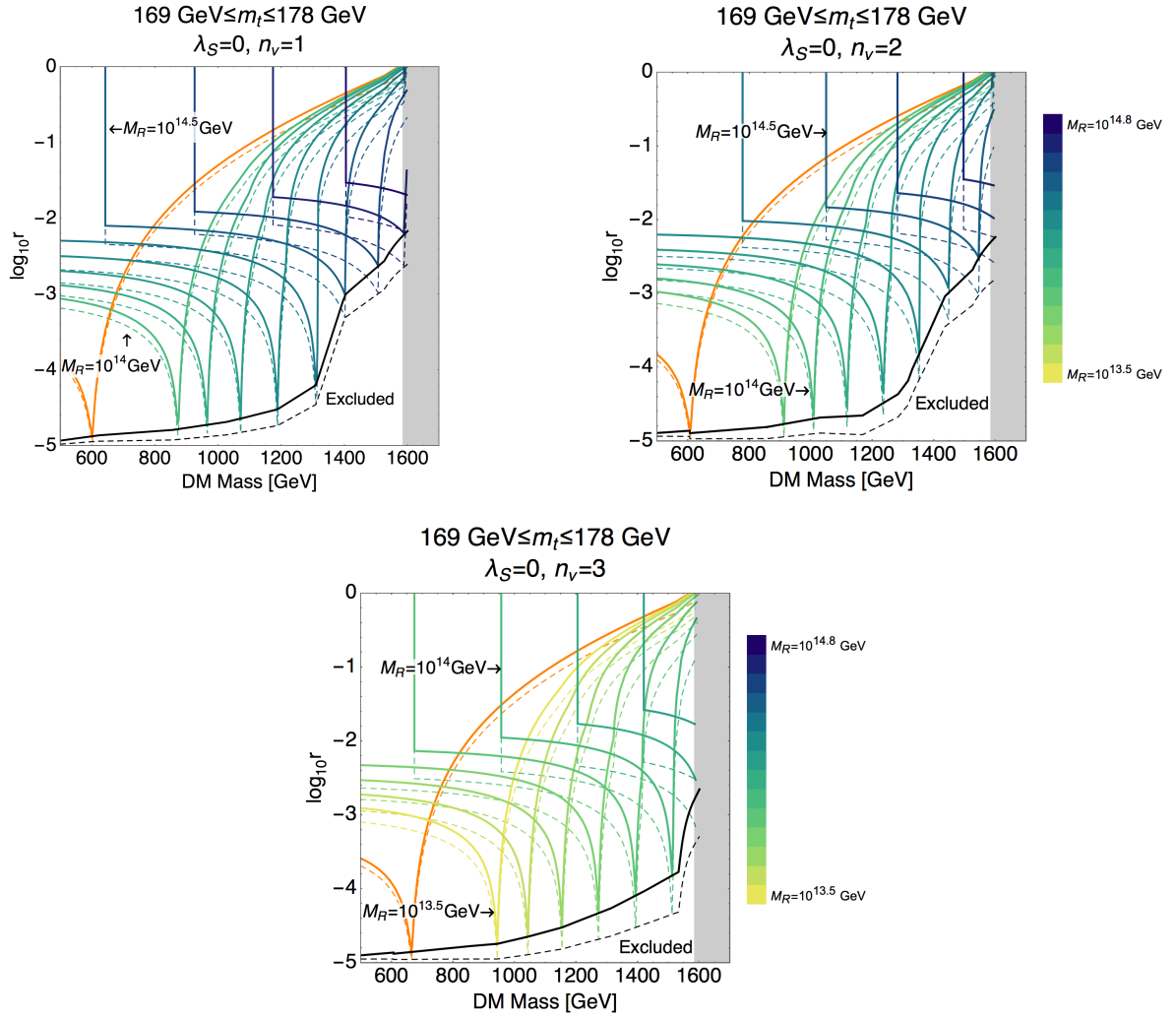


Figure 7: The same plot as in Fig. 6 for  $169 \text{ GeV} < m_t < 178 \text{ GeV}$ .

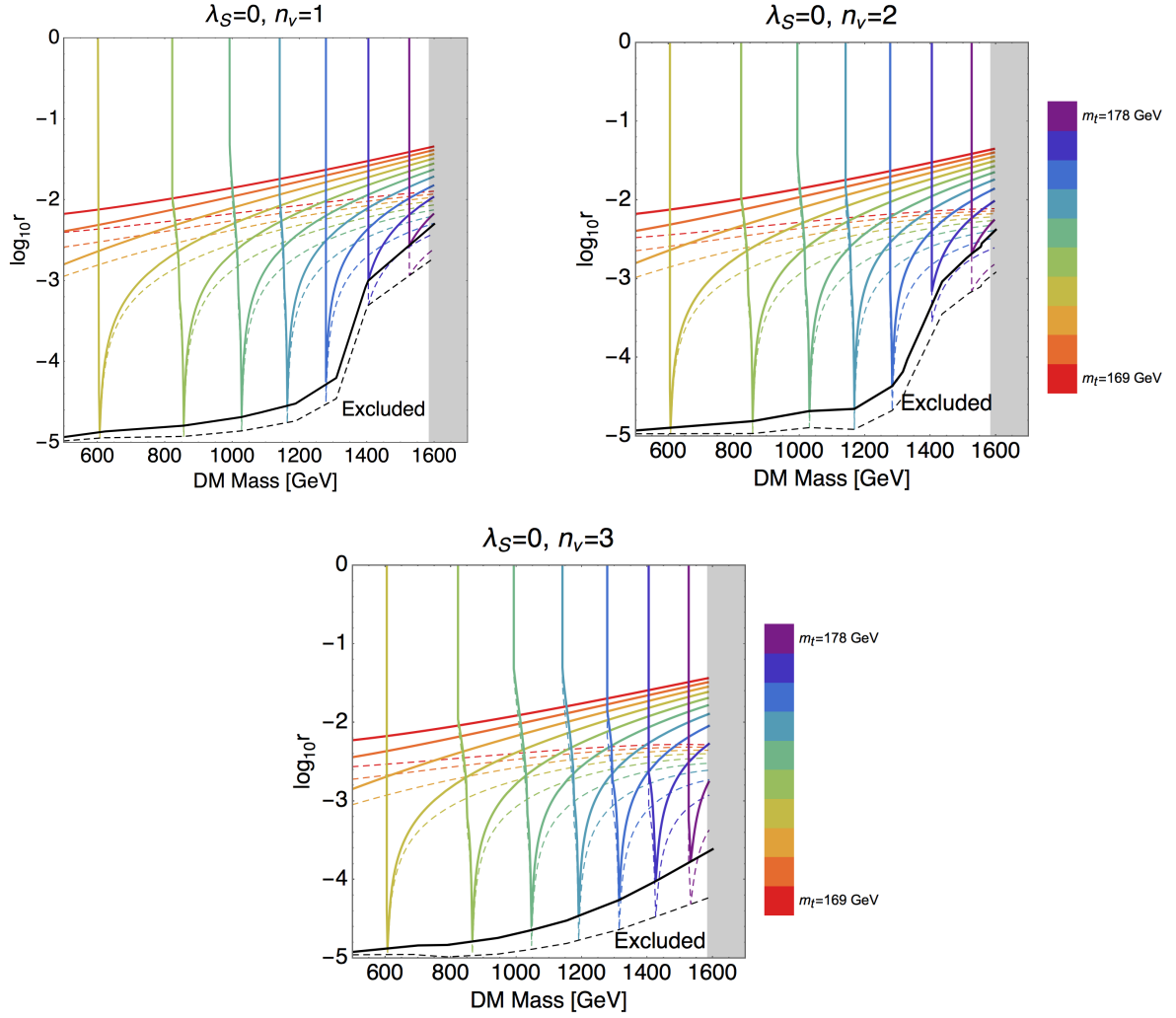


Figure 8: The lower bound on  $r$  for each fixed  $m_t$  (colored) with  $\lambda_S = 0$ . The black line is their envelope, which is identical to the ones in Figs. 6 and 7 except for their right-most boundary where they follow the  $m_t = 176$  GeV (blue) and 178 GeV (purple) lines in this figure, respectively. See the left of Fig. 2 for the corresponding plot without right-handed neutrinos and for the explanation of the shaded region.

## 7 Summary and discussion

We have calculated the lower bound on the tensor-to-scalar ratio,  $r$ , for each given mass of the Higgs-portal  $Z_2$  scalar dark matter,  $m_{\text{DM}}$ , under the simple assumption that the extrapolation of the Higgs-field direction plays the role of inflaton at  $\varphi > \Lambda$ . The advantage of our approach is that we may obtain the lower bound on  $r$  without knowing any detail of the high-scale physics.

In the case without the heavy right-handed neutrinos, we have obtained the theoretical bounds on (i) the DM mass  $m_{\text{DM}} \lesssim 1.1 \text{ TeV}$ , (ii) the tensor-to-scalar ratio  $r \gtrsim 4 \times 10^{-3}$ , and (iii) the pole mass of the top quark  $171 \text{ GeV} < m_t < 175 \text{ GeV}$  from the current observational constraints  $r < 0.09$  and  $m_{\text{DM}} \gtrsim 750 \text{ GeV}$ . We see that (i) and (ii) are rather stringent and are well within the near-future detection.

With the heavy right-handed neutrinos, we obtain the wider allowed region in the  $r$ - $m_{\text{DM}}$  plane,  $r \gtrsim 10^{-5}$  and  $m_{\text{DM}} \lesssim 1.6 \text{ TeV}$ , if we allow a three-parameter tuning. Although the region  $r \lesssim 10^{-3}$  is hard for the planned near-future observations, we may still explore it in combination with the HL-LHC and future neutrino experiments because of the strong correlations between  $m_t$ ,  $m_{\text{DM}}$  and the right-handed neutrino mass  $M_{\text{R}}$ .

The lower bound on  $r$  may slightly be affected when we relax the positivity condition on the Higgs potential by e.g. taking into account the thermal correction or by replacing it with the vacuum meta-stability. Because our bound is coming from the maximum value of effective Higgs potential, rather than the minimum, the lower bound on  $r$  would be reduced only by a factor of few even if we allow the negative value of the potential minimum of the order of the height of the potential maximum. Of course we should make sure that finally the EW vacuum is chosen in the late time in such a case.

In our RG analysis, we have assumed that all the fields are massless.<sup>11</sup> In general, the non-minimal couplings  $\xi\varphi^2 R$  and  $\xi_S S^2 R$  cause the mass terms of the order of  $\xi H^2 \varphi^2$  and  $\xi_S H^2 S^2$ , respectively. Under a classical field value  $\varphi_{\text{cl}}$ , we get

$$\xi H^2 \varphi^2 \sim \xi \lambda \frac{\varphi_{\text{cl}}^4}{M_{\text{P}}^2} \varphi^2, \quad \xi_S H^2 S^2 \sim \xi_S \lambda \frac{\varphi_{\text{cl}}^4}{M_{\text{P}}^2} S^2. \quad (16)$$

Such effective masses  $\sqrt{\xi\lambda}\varphi_{\text{cl}}^2/M_{\text{P}}$  and  $\sqrt{\xi_S\lambda}\varphi_{\text{cl}}^2/M_{\text{P}}$  are smaller enough than  $\mu \sim \varphi_{\text{cl}}$  since we consider the non-minimal couplings  $\xi, \xi_S \lesssim 10^2$  and the small quartic coupling  $\lambda \ll 10^{-1}$  in the region  $\varphi_{\text{cl}} \lesssim 10^{17} \text{ GeV}$ .

It would be interesting to investigate the cosmology of our scenario after the inflation. For example, the Higgs field may be trapped at a false vacuum, and a mini inflation may results from it, depending on the initial condition at the end of the main inflation.<sup>12</sup> Afterwards, the true-vacuum bubbles should be created by the tunneling process, and the first order phase transition be completed by the bubble collision, which generates primordial gravitational waves and black holes. In addition, if the Higgs potential has an inflection point, the scalar perturbations could be enhanced, depending on how the slow-roll condition is well satisfied there, and could lead to another mechanism of the formation of primordial black holes. We hope to return to these issues in the future.

<sup>11</sup> The right-handed neutrinos are regarded massless at  $\mu \sim \varphi_{\text{cl}} \gtrsim M_{\text{R}}$ .

<sup>12</sup> In this case, the dynamics of the Higgs field becomes chaotic in the sense that it is sensitive to the initial condition at the end of the main inflation.

## Acknowledgement

We thank Tomohiro Abe, Xiangdong Ji, Kiyoharu Kawana, Jinsu Kim, Tae Geun Kim, Seong Chan Park, and Stanislav Rusak for useful comments. The work of Y.H., H.K., and K.O. are supported in part by JSPS KAKENHI Grant Nos. 16J06151 (YH), 16K05322 (HK), and 15K05053 (KO), respectively.

## A Renormalization group equations

We have calculated the lower bound on  $r$  as follows:

1. Solve the RGEs (20)–(27) (shown in the end of this section) for given parameters.<sup>13</sup> The effects from right-handed neutrino is introduced only at high energy scale  $\varphi \geq M_R$ : We set  $n_\nu = 0$  and  $M_R = 0$  in  $\varphi < M_R$ . As the boundary condition to solve the RGEs, we have used Eqs. (11)–(15) in [25] and the values in Table 6.
2. Calculate the one-loop effective Higgs potential

$$V_{\varphi \leq \Lambda} = \frac{\lambda_{\text{eff}}}{4} \varphi^4 \quad (17)$$

where

$$\lambda_{\text{eff}} := e^{4\Gamma} \left[ \lambda + \frac{1}{16\pi^2} \left\{ -3y_t^4 \left( \ln \frac{y_t^2}{2} - \frac{3}{2} + 2\Gamma \right) + \frac{3g_2^2}{8} \left( \ln \frac{g_2^2}{4} - \frac{5}{6} + 2\Gamma \right) + \frac{3(g_Y^2 + g_2^2)^2}{16} \left( \ln \frac{g_Y^2 + g_2^2}{4} - \frac{5}{6} + 2\Gamma \right) - n_\nu y_\nu^4 \ln \left( \frac{M_R + \sqrt{M_R^2 + 4y_\nu^2 \varphi^2}}{2\sqrt{M_R^2 + \varphi^2}} \right) \right\} \right] \quad (18)$$

is the effective Higgs-self coupling.<sup>14</sup> We set  $\mu = \varphi$  when we calculate  $\lambda_{\text{eff}}$ ; see [23, 42] for the details about the renormalization scale  $\mu$  of  $\lambda_{\text{eff}}$ . The one-loop wave-function

<sup>13</sup> In this section, we omit the argument of the couplings but it should be understood that they are not the values at  $\mu = m_t$ ; see footnote 2.

<sup>14</sup> The last term in the braces is introduced to *naively* take into account the effect of the neutrino loop on the effective potential. We have checked that its effect is at most few percent.

	Value	Reference
Planck mass $M_P$	$2.4353 \times 10^{18}$ GeV	[32]
Higgs mass	125.09 GeV	[32]
$Z$ bozon mass $M_Z$	91.1876 GeV	[32]
$\alpha_3(M_Z)$	0.1184	[11]
The expectation value of the Higgs field $v$	246 GeV	[32]

Table 6: Boundary condition for the RGEs.

renormalization

$$\Gamma(\varphi) = \int_{m_t}^{\varphi} \frac{1}{16\pi^2} \left( \frac{9}{4}g_2^2 + \frac{3}{4}g_Y^2 - 3y_t^2 - n_\nu y_\nu^2 \right) d \ln \mu \quad (19)$$

is neglected due to the calculation cost; its error is estimated as stated below.

3. Change the parameters using the false position method until the value of the potential minimum becomes sufficiently close to zero.
4. Calculate the maximum value of potential and obtain  $r_{\text{bound}}$  via Eq. (5).
5. Obtain the value of  $\Gamma(\varphi)$  at  $\varphi = \Lambda$  and use it to estimate the deviation at the potential maximum. This is most conservative because  $\Gamma(\varphi)$  becomes largest at  $\varphi = \Lambda$ . This estimation corresponding to the dashed lines in the figures.

We have obtained the RGEs for arbitrary  $n_\nu$  combining the  $n_\nu = 1$  RGEs [43] and the  $n_\nu = 3$  ones [44]:

$$\frac{dg_Y}{d \ln \mu} = \frac{1}{16\pi^2} \frac{41}{6} g_Y^3 + \frac{g_Y^3}{(16\pi^2)^2} \left( \frac{199}{18} g_Y^2 + \frac{9}{2} g_2^2 + \frac{44}{3} g_3^2 - \frac{17}{6} y_t^2 - \frac{n_\nu}{2} y_\nu^2 \right), \quad (20)$$

$$\frac{dg_2}{d \ln \mu} = -\frac{1}{16\pi^2} \frac{19}{6} g_2^3 + \frac{g_2^3}{(16\pi^2)^2} \left( \frac{3}{2} g_Y^2 + \frac{35}{6} g_2^2 + 12g_3^2 - \frac{3}{2} y_t^2 - \frac{n_\nu}{2} y_\nu^2 \right), \quad (21)$$

$$\frac{dg_3}{d \ln \mu} = -\frac{7}{16\pi^2} g_3^3 + \frac{g_3^3}{(16\pi^2)^2} \left( \frac{11}{6} g_Y^2 + \frac{9}{2} g_2^2 - 26g_3^2 - 2y_t^2 \right), \quad (22)$$

$$\begin{aligned} \frac{dy_t}{d \ln \mu} &= \frac{y_t}{16\pi^2} \left( \frac{9}{2} y_t^2 + n_\nu y_\nu^2 - \frac{17}{12} g_Y^2 - \frac{9}{4} g_2^2 - 8g_3^2 \right) + \frac{y_t}{(16\pi^2)^2} \left\{ -12y_t^2 - \frac{9n_\nu}{4} y_\nu^4 - \frac{9n_\nu}{4} y_t^2 y_\nu^2 \right. \\ &\quad + 6\lambda^2 + \frac{1}{4} \kappa^2 - 12\lambda y_t^2 + g_Y^2 \left( \frac{131}{16} y_t^2 + \frac{5n_\nu}{8} y_\nu^2 \right) + g_2^2 \left( \frac{225}{16} y_t^2 + \frac{5n_\nu}{8} y_\nu^2 \right) + 36g_3^2 y_t^2 \\ &\quad \left. + \frac{1187}{216} g_Y^4 - \frac{23}{4} g_2^4 - 108g_3^4 - \frac{3}{4} g_Y^2 g_2^2 + 9g_2^2 g_3^2 + \frac{19}{9} g_3^2 g_Y^2 \right\}, \quad (23) \end{aligned}$$

$$\begin{aligned} \frac{dy_\nu}{d \ln \mu} &= \frac{y_\nu}{16\pi^2} \left\{ \left( n_\nu + \frac{3}{2} \right) y_\nu^2 + 3y_t^2 - \frac{3}{4} g_Y^2 - \frac{9}{4} g_2^2 \right\} + \frac{y_\nu}{(16\pi^2)^2} \left\{ - \left( \frac{9n_\nu}{2} - \frac{3}{2} \right) y_\nu^4 - \frac{27}{4} y_t^4 \right. \\ &\quad - \frac{27}{4} y_t^2 y_\nu^2 + 6\lambda^2 + \frac{1}{4} \kappa^2 - 12\lambda y_\nu^2 + g_Y^2 \left( \left( \frac{5n_\nu}{8} + \frac{93}{16} \right) y_\nu^2 + \frac{85}{24} y_t^2 \right) \\ &\quad \left. + g_2^2 \left( \left( \frac{15n_\nu}{8} + \frac{135}{16} \right) y_\nu^2 + \frac{45}{8} y_t^2 \right) + 20g_3^2 y_t^2 + \frac{35}{24} g_Y^4 - \frac{23}{4} g_2^4 - \frac{9}{4} g_Y^2 g_2^2 \right\}, \quad (24) \end{aligned}$$

$$\begin{aligned} \frac{d\lambda}{d \ln \mu} &= \frac{1}{16\pi^2} \left( \frac{1}{2} \kappa^2 + 24\lambda^2 - 3g_Y^2 \lambda - 9g_2^2 \lambda + 4n_\nu \lambda y_\nu^2 + \frac{3}{8} g_Y^4 + \frac{3}{4} g_Y^2 g_2^2 + \frac{9}{8} g_2^4 + 12\lambda y_t^2 - 6y_t^4 - 2n_\nu y_\nu^4 \right) \\ &\quad + \frac{1}{(16\pi^2)^2} \left\{ -2\kappa^3 - 5\kappa^2 \lambda - 312\lambda^3 + 36\lambda^2 (g_Y^2 + 3g_2^2) - \lambda \left( \frac{629}{24} g_Y^4 - \frac{39}{4} g_Y^2 g_2^2 + \frac{73}{8} g_2^4 \right) \right. \\ &\quad + \frac{305}{16} g_2^6 - \frac{289}{48} g_Y^2 g_2^4 - \frac{559}{48} g_Y^4 g_2^2 - \frac{379}{48} g_Y^6 - 32g_3^2 y_t^4 - \frac{8}{3} g_Y^2 y_t^4 - \frac{9}{4} g_2^4 y_t^2 - \frac{3n_\nu}{4} g_2^4 y_\nu^2 \\ &\quad + \lambda y_t^2 \left( \frac{85}{6} g_Y^2 + \frac{45}{2} g_2^2 + 80g_3^2 \right) + \lambda y_\nu^2 \left( \frac{5n_\nu}{2} g_Y^2 + \frac{15n_\nu}{2} g_2^2 \right) + g_Y^2 y_t^2 \left( -\frac{19}{4} g_Y^2 + \frac{21}{2} g_2^2 \right) \\ &\quad \left. - g_Y^2 y_\nu^2 \left( \frac{n_\nu}{4} g_Y^2 + \frac{n_\nu}{2} g_2^2 \right) - 144\lambda^2 y_t^2 - 48n_\nu y_\nu^2 - 3\lambda y_t^4 - n_\nu \lambda y_\nu^4 + 30y_t^6 + 10n_\nu y_\nu^6 \right\}, \quad (25) \end{aligned}$$

$$\begin{aligned}
\frac{d\kappa}{d\ln\mu} = & \frac{\kappa}{16\pi^2} \left( 12\lambda + \lambda_S + 4\kappa + 6y_t^2 + 2n_\nu y_\nu^2 - \frac{3}{2}g_Y^2 - \frac{9}{2}g_2^2 \right) + \frac{\kappa}{(16\pi^2)^2} \left\{ -\frac{21}{2}\kappa^2 \right. \\
& - 72\kappa\lambda - 60\lambda^2 - 6\kappa\lambda_S - \frac{5}{6}\lambda_S^2 - y_t^2(12\kappa + 72\lambda) - 4n_\nu\kappa y_\nu^2 - 24n_\nu\lambda y_\nu^2 \\
& - \frac{27}{2}y_t^4 - \frac{9n_\nu}{2}y_\nu^4 + g_Y^2(\kappa + 24\lambda) + g_2^2(3\kappa + 72\lambda) + y_t^2 \left( \frac{85}{12}g_Y^2 + \frac{45}{4}g_2^2 + 40g_3^2 \right) \\
& \left. + y_\nu^2 \left( \frac{5n_\nu}{4}g_Y^2 + \frac{15n_\nu}{4}g_2^2 \right) + \frac{557}{48}g_Y^4 - \frac{145}{16}g_2^4 + \frac{15}{8}g_Y^2g_2^2 \right\}, \tag{26}
\end{aligned}$$

$$\begin{aligned}
\frac{d\lambda_S}{d\ln\mu} = & \frac{1}{16\pi^2} (3\lambda_S^2 + 12\kappa^2) + \frac{1}{(16\pi^2)^2} \left\{ -\frac{17}{3}\lambda_S^3 \right. \\
& \left. - 20\kappa^2\lambda_S - 48\kappa^3 - 72\kappa^2y_t^2 - 24n_\nu\kappa^2y_\nu^2 + 24\kappa^2g_Y^2 + 72\kappa^2g_2^2 \right\}. \tag{27}
\end{aligned}$$

## B Explaining the form of envelope by potential shape

In this section, we explain the shape of envelopes denoted by the black or colored-thick line in the figures.

Let us start with the case without heavy right-handed neutrino (the left of Fig. 2). At the minimum point of envelope, the maximum value of the Higgs potential becomes smallest. In Fig. 9, we show the shape of potential near this point. At this minimum point, the height at the local maximum (at  $\varphi \simeq 5 \times 10^{16}$  GeV in the case of Fig. 9) becomes identical to the height at  $\varphi = \Lambda$ . If the local potential minimum (at  $\varphi = 9 \times 10^{16}$  GeV in the case of Fig. 9) is moved left, then the height at  $\varphi = \Lambda$  becomes larger, while moved right, the height at the local maximum becomes larger. The left of the minimum point of the envelope is governed by the local maximum of the potential, while the right by the value at  $\varphi = \Lambda$ .

Now we turn to the case with right-handed neutrinos. The envelope is denoted by the colored thick line in Figs. 3–5. We note that there is one more (hardly seeable) discontinuity in each envelope, which can be seen in Fig. 7, where the envelopes are summarized in a single panel with the same colors: The discontinuity is located, e.g. in the  $n_\nu = 1$  panel, at  $(m_{\text{DM}}, \log_{10} r) \sim (1050 \text{ GeV}, -1.5)$  for  $M_{\text{R}} = 10^{14}$  GeV,  $(1100 \text{ GeV}, -1.7)$  for  $M_{\text{R}} = 10^{14.1}$  GeV,  $(1150 \text{ GeV}, -2)$  for  $M_{\text{R}} = 10^{14.2}$  GeV, and  $(1220 \text{ GeV}, -2.6)$  for  $M_{\text{R}} = 10^{14.3}$  GeV. This is because the Higgs potential has two local minima in general: The one at higher (lower)

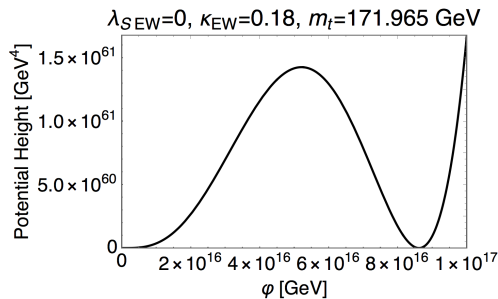


Figure 9: The shape of Higgs potential with the values of  $m_t$  and  $m_{\text{DM}}(\kappa)$  that corresponds to a point near the minimum of the envelope in the left of Fig. 2.

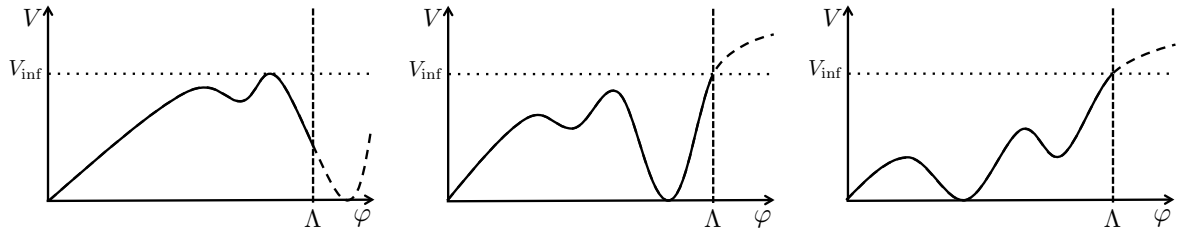


Figure 10: Left: Typical potential shape when its minimum is at  $\varphi > \Lambda$ . Center: Typical potential shape when the minimum at larger  $\varphi$  gives lower height. Right: Typical potential shape when the minimum at smaller  $\varphi$  gives lower height.

$\varphi$  is due to the neutrino (top quark) contribution.<sup>15</sup> There are the following three kinds of potential shapes:

- (i) On the left side of the minimum of each envelope, the potential minimum at higher  $\varphi$  is located at  $\varphi > \Lambda$ ; see the left of Fig. 10.
- (ii) In between the minimum and the discontinuity of each envelope, there are two potential minima and the height of the one at larger  $\varphi$  is smaller; see the center of Fig. 10.
- (iii) On the right side of the discontinuity of each envelope, there are two potential minima and the height of the one at lower  $\varphi$  is smaller; see the right of Fig. 10.

These two potential minima are degenerate on the black line in Figs. 6 and 7, and the cases (ii) and (iii) become identical.

We can see this discontinuity from another point of view in Fig. 11. The left end of each solid rainbow-colored line for  $m_t \lesssim 174$  GeV is the  $M_R \rightarrow 0$  limit, and should be the same as the black line in Fig. 2 of  $n_\nu = 0$ . However, they do not touch the black  $n_\nu = 0$  line for  $m_t \gtrsim 175$  GeV. This is because there arises the two local minima of the potential as in the case (iii): The minimum at lower  $\varphi$  can be tuned to be zero by the top-quark contribution, and the neutrino contribution may produce the minimum at higher  $\varphi$ , which allows to reduce the maximum potential height freely. The gray line in Fig. 11 links the left ends of the solid rainbow-colored lines for the region  $m_t \gtrsim 175$  GeV, and is the same as the line joining the discontinuities mentioned above.

Finally, we explain why the envelope in Fig. 11 (black, lower) is bent in the large  $m_{DM}$  region. At the point where the gray line touches the envelope (black, lower), the potential height of the two degenerate minima becomes zero.<sup>16</sup> On its right side, the case (i) is realized, and the maximum potential height becomes much larger than the cases (ii) and (iii) with the two minima.

<sup>15</sup> Here we let the word “minimum” also stands for mere a concavity, namely, even when it is not really a minimum.

<sup>16</sup> At this point, the EW and these two vacua are all degenerate to (nearly) zero, and the vacuum with highest  $\varphi$  is located at  $\varphi = \Lambda$ . This point may be interesting in term of the multiple-point principle [39, 40, 41].

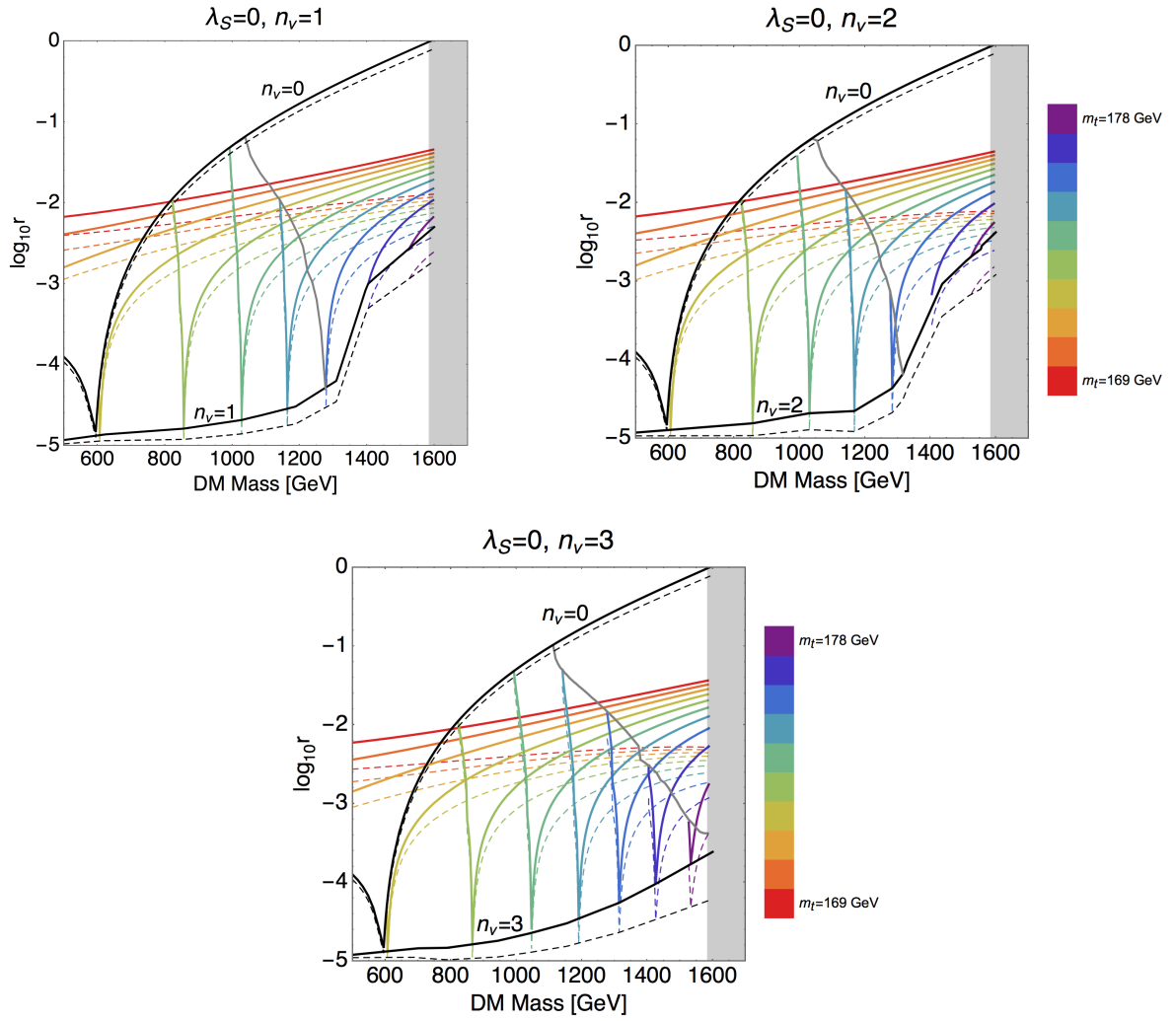


Figure 11: The same plot as in Fig. 8. The black  $n_\nu = 0$  line in Fig. 2 is also superimposed. The gray line show the location of the discontinuity explained in the text, and links the left ends of the rainbow-colored lines for  $m_t \gtrsim 175$  GeV.

## References

- [1] Planck, P. A. R. Ade et al., *Planck 2015 results. XIII. Cosmological parameters*, *Astron. Astrophys.* **594** (2016), A13, 1502.01589.
- [2] D. S. Salopek, J. R. Bond, and J. M. Bardeen, *Designing Density Fluctuation Spectra in Inflation*, *Phys. Rev.* **D40** (1989), 1753.
- [3] F. Bezrukov and M. Shaposhnikov, *The Standard Model Higgs boson as the inflaton*, *Phys.Lett.* **B659** (2008), 703–706, 0710.3755.
- [4] M. Holthausen, K. S. Lim, and M. Lindner, *Planck scale Boundary Conditions and the Higgs Mass*, *JHEP* **1202** (2012), 037, 1112.2415.
- [5] F. Bezrukov, M. Y. Kalmykov, B. A. Kniehl, and M. Shaposhnikov, *Higgs Boson Mass and New Physics*, *JHEP* **1210** (2012), 140, 1205.2893.
- [6] G. Degrassi, S. Di Vita, J. Elias-Miro, J. R. Espinosa, G. F. Giudice, G. Isidori, and A. Strumia, *Higgs mass and vacuum stability in the Standard Model at NNLO*, *JHEP* **08** (2012), 098, 1205.6497.
- [7] S. Alekhin, A. Djouadi, and S. Moch, *The top quark and Higgs boson masses and the stability of the electroweak vacuum*, *Phys.Lett.* **B716** (2012), 214–219, 1207.0980.
- [8] I. Masina, *The Higgs boson and Top quark masses as tests of Electroweak Vacuum Stability*, *Phys.Rev.* **D87** (2013), 053001, 1209.0393.
- [9] Y. Hamada, H. Kawai, and K.-y. Oda, *Bare Higgs mass at Planck scale*, *Phys. Rev.* **D87** (2013), no. 5, 053009, 1210.2538, [Erratum: *Phys. Rev.* **D89**, no.5, 059901(2014)].
- [10] F. Jegerlehner, *The Standard model as a low-energy effective theory: what is triggering the Higgs mechanism?*, (2013), 1304.7813.
- [11] D. Buttazzo, G. Degrassi, P. P. Giardino, G. F. Giudice, F. Sala, A. Salvio, and A. Strumia, *Investigating the near-criticality of the Higgs boson*, *JHEP* **12** (2013), 089, 1307.3536.
- [12] V. Branchina and E. Messina, *Stability, Higgs Boson Mass and New Physics*, *Phys.Rev.Lett.* **111** (2013), 241801, 1307.5193.
- [13] A. Kobakhidze and A. Spencer-Smith, *The Higgs vacuum is unstable*, (2014), 1404.4709.
- [14] A. Spencer-Smith, *Higgs Vacuum Stability in a Mass-Dependent Renormalisation Scheme*, (2014), 1405.1975.
- [15] V. Branchina, E. Messina, and A. Platania, *Top mass determination, Higgs inflation, and vacuum stability*, (2014), 1407.4112.
- [16] V. Branchina, E. Messina, and M. Sher, *The lifetime of the electroweak vacuum and sensitivity to Planck scale physics*, (2014), 1408.5302.

- [17] A. V. Bednyakov, B. A. Kniehl, A. F. Pikelner, and O. L. Veretin, *Stability of the Electroweak Vacuum: Gauge Independence and Advanced Precision*, Phys. Rev. Lett. **115** (2015), no. 20, 201802, 1507.08833.
- [18] Y. Hamada, H. Kawai, and K.-y. Oda, *Minimal Higgs inflation*, PTEP **2014** (2014), 023B02, 1308.6651.
- [19] Y. Hamada, H. Kawai, and K.-y. Oda, *Eternal Higgs inflation and the cosmological constant problem*, Phys. Rev. **D92** (2015), 045009, 1501.04455.
- [20] Y. Hamada, H. Kawai, K.-y. Oda, and S. C. Park, *Higgs inflation still alive*, Phys.Rev.Lett. **112** (2014), 241301, 1403.5043.
- [21] J. L. Cook, L. M. Krauss, A. J. Long, and S. Sabharwal, *Is Higgs Inflation Dead?*, Phys.Rev. **D89** (2014), 103525, 1403.4971.
- [22] Bezrukov, Fedor and Shaposhnikov, Mikhail, *Higgs inflation at the critical point*, (2014), 1403.6078.
- [23] Y. Hamada, H. Kawai, K.-y. Oda, and S. C. Park, *Higgs inflation from Standard Model criticality*, Phys. Rev. **D91** (2015), 053008, 1408.4864.
- [24] J. M. Cline, K. Kainulainen, P. Scott, and C. Weniger, *Update on scalar singlet dark matter*, Phys. Rev. **D88** (2013), 055025, 1306.4710, [Erratum: Phys. Rev.D92,no.3,039906(2015)].
- [25] Y. Hamada, H. Kawai, and K.-y. Oda, *Predictions on mass of Higgs portal scalar dark matter from Higgs inflation and flat potential*, JHEP **07** (2014), 026, 1404.6141.
- [26] XENON, E. Aprile et al., *First Dark Matter Search Results from the XENON1T Experiment*, (2017), 1705.06655.
- [27] LUX, D. S. Akerib et al., *Results from a search for dark matter in the complete LUX exposure*, Phys. Rev. Lett. **118** (2017), no. 2, 021303, 1608.07648.
- [28] PandaX-II, : et al., *Dark Matter Results From 54-Ton-Day Exposure of PandaX-II Experiment*, (2017), 1708.06917.
- [29] P. Minkowski,  $\mu \rightarrow e\gamma$  at a Rate of One Out of  $10^9$  Muon Decays?, Phys. Lett. **67B** (1977), 421–428.
- [30] T. Yanagida, in *Proceedings of the Workshop on Unified Theory and Baryon Number of the Universe*, edited by O. Sawada and A. Sugamoto (KEK, Tokyo, 1979), p. 95; M. Gell-Mann, P. Ramond, and R. Slanski, in *Supergravity*, edited by P. van Nieuwenhuizen and D. Freedman (North-Holland, Amsterdam, 1979) arXiv:1306.4669; S. L. Glashow, in *Proceedings of the Cargèse Summer Institute on Quarks and Leptons*, Cargèse, July 9–29, 1979, eds. M. Lévy et al. (Plenum, 1980, New York), p. 707; R. N. Mohapatra and G. Senjanovic, *Neutrino Mass and Spontaneous Parity Violation*, Phys. Rev. Lett. **44** (1980) 912.
- [31] Planck, P. A. R. Ade et al., *Planck 2015 results. XX. Constraints on inflation*, Astron. Astrophys. **594** (2016), A20, 1502.02114.

- [32] Particle Data Group, C. Patrignani et al., *Review of Particle Physics*, Chin. Phys. **C40** (2016), no. 10, 100001.
- [33] G. Cortiana, *Top-quark mass measurements: review and perspectives*, Rev. Phys. **1** (2016), 60–76, 1510.04483.
- [34] POLARBEAR, Y. Inoue et al., *POLARBEAR-2: an instrument for CMB polarization measurements*, Proc. SPIE Int. Soc. Opt. Eng. **9914** (2016), 99141I, 1608.03025.
- [35] T. Matsumura et al., *Mission design of LiteBIRD*, (2013), 1311.2847, [J. Low. Temp. Phys.176,733(2014)].
- [36] CORE, J. Delabrouille et al., *Exploring Cosmic Origins with CORE: Survey requirements and mission design*, (2017), 1706.04516.
- [37] F. Capozzi, E. Di Valentino, E. Lisi, A. Marrone, A. Melchiorri, and A. Palazzo, *Global constraints on absolute neutrino masses and their ordering*, (2017), 1703.04471.
- [38] CMS Collaboration, *Updates on Projections of Physics Reach with the Upgraded CMS Detector for High Luminosity LHC*, (2016), <https://cds.cern.ch/record/2221747>.
- [39] C. D. Froggatt and H. B. Nielsen, *Standard model criticality prediction: Top mass  $173 \pm 5$ -GeV and Higgs mass  $135 \pm 9$ -GeV*, Phys. Lett. **B368** (1996), 96–102, hep-ph/9511371.
- [40] C. Froggatt, H. B. Nielsen, and Y. Takanishi, *Standard model Higgs boson mass from borderline metastability of the vacuum*, Phys.Rev. **D64** (2001), 113014, hep-ph/0104161.
- [41] H. B. Nielsen, *PREDicted the Higgs Mass*, (2012), 94–126, 1212.5716.
- [42] Y. Hamada, H. Kawai, Y. Nakanishi, and K.-y. Oda, *Meaning of the field dependence of the renormalization scale in Higgs inflation*, Phys. Rev. **D95** (2017), no. 10, 103524, 1610.05885.
- [43] N. Haba, H. Ishida, and R. Takahashi, *Higgs inflation and Higgs portal dark matter with right-handed neutrinos*, PTEP **2015** (2015), no. 5, 053B01, 1405.5738.
- [44] K. Kawana, *Multiple Point Principle of the Standard Model with Scalar Singlet Dark Matter and Right Handed Neutrinos*, PTEP **2015** (2015), 023B04, 1411.2097.